

Journal of Biomedical Optics

BiomedicalOptics.SPIEDigitalLibrary.org

Characterization of the Cerenkov scatter function: a convolution kernel for Cerenkov light dosimetry

Eric Brost
Yoichi Watanabe

SPIE.

Eric Brost, Yoichi Watanabe, "Characterization of the Cerenkov scatter function: a convolution kernel for Cerenkov light dosimetry," *J. Biomed. Opt.* **23**(10), 105007 (2018), doi: 10.1117/1.JBO.23.10.105007.

Characterization of the Cerenkov scatter function: a convolution kernel for Cerenkov light dosimetry

Eric Brost* and Yoichi Watanabe

University of Minnesota, Department of Radiation Oncology, Minneapolis, Minnesota, United States

Abstract. Cerenkov light is created in clinical applications involving high-energy radiation such as in radiation therapy. There is considerable interest in using Cerenkov light as a means to perform *in vivo* dosimetry during radiation therapy; however, a better understanding of the light-to-dose relationship is needed. One such method to solve this relationship is that of a deconvolution formulation, which relies on the Cerenkov scatter function (CSF). The CSF describes the creation of Cerenkov photons by a pencil beam of high-energy radiation, and the subsequent scattering that occurs before emission from the irradiated medium surface. This study investigated the dependence of the CSF on common radiation beam parameters (beam energy and incident angle) and the type of irradiated medium. An analytical equation with fitting coefficients of the CSF was obtained for common beam energies in a stratified skin model and optical phantom. Perturbation analysis was performed to investigate the dependence of the deconvolved Cerenkov images on the full-width at half-maximum and amplitude of the CSF. The irradiated material and beam angle had a large impact on the deconvolution process, whereas the beam energy had little effect. © 2018 Society of Photo-Optical Instrumentation Engineers (SPIE) [DOI: 10.1117/1.JBO.23.10.105007]

Keywords: Cerenkov radiation; tissue optics; Monte Carlo; radiation dosimetry.

Paper 180406RR received Jul. 4, 2018; accepted for publication Oct. 1, 2018; published online Oct. 30, 2018.

1 Introduction

External beam radiation therapy (EBRT) is the most common form of radiation therapy techniques. To deliver EBRT, a linear accelerator (linac) is used to accelerate electrons to high energies and then treat a patient with either the accelerated electrons or bremsstrahlung photons. The radiation beams are collimated so that radiation dose is maximized to a treatment volume within the patient and minimized to the surrounding tissues and organs. The treatment volume may be in a superficial area or deep within the body depending on the type and extent of the cancer. Some dose is inevitably deposited within normal tissues due to the flux of radiation passing through these tissues on its path to the treatment volume. The dose to both normal tissues and treatment volumes is calculated based upon computed-tomography (CT) data using semianalytical methods or Monte Carlo (MC) simulation.¹ These methods are used to calculate dose within the three-dimensional model of the patient by considering the heterogeneity of tissues. The dose is rarely measured *in vivo* during patient treatment. When it is performed, *in vivo* measurement is typically done with point-like dosimeters such as thermoluminescent dosimeters or optically stimulated luminescence dosimeters, which measure the dose only at a point on the patient's skin surface. A two-dimensional (2-D) *in vivo* dose measurement method could be helpful for evaluating the accuracy of the prescribed treatment, monitoring hot spots of dose deposition, and improving the therapeutic outcomes of the radiation therapy.² However, there is no method that can perform this type of dosimetry in real time with sufficient accuracy.

Radiation treatment beams produce electrons that are responsible for dose deposition in a medium. Above a certain energy threshold, these charged particles will travel faster than the phase velocity of light within the medium, and emit Cerenkov photons as visible light along their path of travel.³ The spectrum

and amount of Cerenkov light produced are governed by the Frank–Tamm formula.⁴ Recently, there have been numerous studies showing the applications of Cerenkov photon imaging in radiation therapy.^{5–15} There is currently much interest in using Cerenkov photons during EBRT as a means to estimate the dose delivered by the treatment in 2-D and in real time.^{16–19} However, a better understanding of the complex relationship between Cerenkov photon emission and dose deposition is needed to improve the dose prediction accuracy of this method.¹⁶ The light-to-dose relationship was previously approached as a deconvolution problem.²⁰ Cerenkov photons are emitted in locations corresponding to dose deposition, hence, deconvolution by a light-transfer function can be used to isolate the regions of dose.

In previous studies, a concept known as the Cerenkov scatter function (CSF), which is the collection of all scattered Cerenkov photons that are emitted from the surface of a medium irradiated by a pencil beam (a Dirac- δ function) of high-energy radiation, was introduced.^{20,21} This function can be used to relate a Cerenkov photon image taken during EBRT to the surface fluence of primary particles through a deconvolution relationship.²⁰ The primary beam fluence can then be used to solve for superficial dose deposition using the well-known relationship between beam fluence and the dose scatter function (DSF).¹ In a previous publication,²⁰ we showed the mathematical relationship between Cerenkov photons imaged during EBRT and dose deposition, but did not include a full characterization of the CSF. The mathematical relationship assumed radiation beam angles normal to the irradiated medium surface and shift-invariant transfer functions (i.e., the CSF and DSF). Expansion of this formulation to clinically relevant geometries will go beyond these assumptions, so the relative effects of nonnormal beam angles and shift-variant CSFs must be investigated. In this

*Address all correspondence to: Eric Brost, E-mail: bros0129@umn.edu

paper, the dependence of the CSF on common beam parameters such as photon energy, incident beam angle, and the type of medium is examined through MC simulation. In addition, the errors introduced into the dose distribution obtained by the deconvolution formulation are examined, through perturbation of the amplitude and shape of the CSF and the incident beam angle. This allows us to determine the sensitivity of the deconvolution formulation to those physical parameters.

2 Theory

The CSF is generated by the radiative transport process of Cerenkov photons created by a pencil beam of ionizing radiation incident on a dielectric medium. This definition was previously introduced for the purpose of superficial dosimetry. We refer the reader to Brost and Watanabe²⁰ for the detailed derivation of the integral equations describing the photon transport and the scatter kernels. Here, the equations will be reintroduced using the convolution operator (*) for the sake of clarity. In these equations, a high-energy photon beam is considered as the primary radiation beam. The incident photon beam produces secondary electrons that are responsible for both dose deposition within the medium and creation of Cerenkov photons. A diagram of this physical process is shown in Fig. 1(a). Figure 1(b) shows the location of Cerenkov photon absorption within a light-pigmented skin model for a 6-MV polyenergetic photon beam. As shown, most of the Cerenkov photons will end up being absorbed by the tissue, but a small fraction (~1%) travels toward the surface

and escapes the irradiated medium. An imaging system can be placed outside of the medium to image escaped photons.

The following equation represents the relationship between Cerenkov photons that reach the imaging system and a radiation beam incident on the medium:

$$I(\theta_{\text{obs}}) = J(\boldsymbol{\Omega}) * \text{CSF}(\boldsymbol{\Omega}, \theta_{\text{obs}}) * \text{PSF}, \quad (1)$$

where I is the Cerenkov photon intensity on the sensor of the imaging system, J is the total fluence of the high-energy photon beam with a known energy spectrum entering the medium with an entrance vector of $\boldsymbol{\Omega}$ relative to the surface normal, CSF is the Cerenkov scatter function representing the Cerenkov photons escaping the medium for a pencil beam incident to the surface, and PSF is the point spread function representing the transport of Cerenkov photons from the medium surface to the imaging system. The parameter θ_{obs} is the observation angle of the imaging system relative to the surface normal. $\boldsymbol{\Omega}$ can be broken down into the components: θ_{in} is the angle of entrance vector defined from the surface normal and ϕ is the rotation of the entrance vector about the Z-axis. Equation (1) shows that an image formed by Cerenkov photons due to an incident beam of radiation is a convolution of the surface flux J by both CSF and PSF. For an ideal imaging system, $\text{PSF} = \delta$ and can be ignored.

The CSF can be written as a convolution of the dose-deposition kernel, the DSF, and a kernel called the Cerenkov dose scatter function (CDSF):

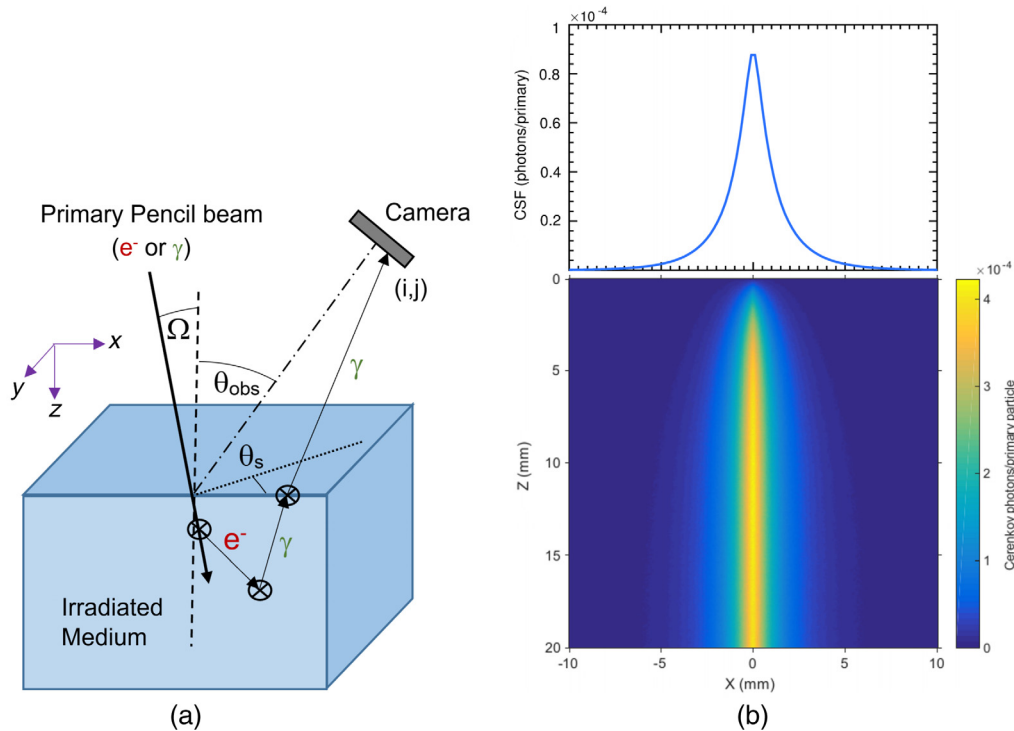


Fig. 1 (a) The coordinate system of the Cerenkov photon creation process and subsequent detection by a camera system. Here, γ (photon) and e^- (electron) represent the primary and secondary particle types involved in the transport of energy, respectively. A primary photon pencil beam is incident on a solid block of medium with angle Ω relative to the surface. The primary photon interacts to create a secondary electron, which then generates a Cerenkov photon. The Cerenkov photon undergoes scattering and absorption within the medium. The CSF is composed of Cerenkov photons that escape the surface. The \otimes symbol represents the interaction points occurring within the medium. (b) A cross section of the absorption map of Cerenkov photons created by a pencil beam incident on a light skin model. Above the absorption map is a cross section of the CSF, scaled to the width of the absorption map. The units of (b) are in Cerenkov photons per primary photon particle.

$$\text{CSF}(\mathbf{\Omega}, \theta_{\text{obs}}) = \text{CDSF}(\mathbf{\Omega}, \theta_{\text{obs}}, d_0) * \text{DSF}(\mathbf{\Omega}, E, d_0). \quad (2)$$

Physically, the CDSF represents the Cerenkov photon production by the secondary electrons and the transport of these photons toward the surface of the medium. Equation (2) indicates that CDSF can be found by deconvolving the CSF with the DSF. Inserting Eq. (2) into Eq. (1), and using the well-known definition of dose deposition ($D = J * \text{DSF}$),¹ I can be expressed as a convolution of D and CDSF as follows:

$$I(\theta_{\text{obs}}) = \text{CDSF}(\mathbf{\Omega}, \theta_{\text{obs}}, d_0) * D(d_0). \quad (3)$$

The aim of this formulation is to find a 2-D dose distribution at a depth d_0 in the medium. The measured Cerenkov photon intensity I can be deconvolved with the known CDSF to obtain the dose profile at the depth d_0 , following Eq. (3). In addition, I can be deconvolved with the known CSF to obtain the total primary fluence profile at the surface of the medium using Eq. (1).

3 Materials and Methods

3.1 Monte Carlo Simulations

GAMOS (version 4.0.0), a Geant4 (version 10.02)-based MC toolkit for medically oriented applications, was used to create simulations to generate the CSFs.²² The Tissue Optical Modeling plugin was used with GAMOS to more accurately simulate the optical physics and handle optical properties.²³ Two simulation studies were done to investigate the dependence of the CSF on various model parameters. The purpose of study (i) was to examine how the CSF changed as a function of incident beam angle. Study (ii) was used to generate CSF fit coefficients for normal beam angles at common treatment energies. Study (ii) utilized the photon energy spectra of 6-, 10-, and 18-MV beams for a TrueBeam linear accelerator (Varian Medical Systems, Palo Alto, California).²⁴ Table 1 shows the beam and model parameters used in each study. The ‘‘GmEMPhysics’’ model was used in all simulations. The step sizes and range cuts for all particles were kept at default in each region. The general photon production threshold was between 0 eV and 1 GeV. The maximum number of Cerenkov photons per step was kept as unlimited.

All CSF simulations involved a pencil beam of radiation incident on a smooth-surfaced, voxelized solid phantom. Each simulation included a geometry file that provided the physical model and optical properties of the phantom. The phantom, a box of $20 \times 20 \text{ cm}^2$ area and 10-cm depth, was placed inside of an empty air volume composed of

Table 1 The simulation parameters for MC studies (i) and (ii). These studies varied the beam angle, energy, and irradiated medium to measure the relative effects on the CSF. Beam energies used were either monoenergetic (mono.) or polyenergetic (poly.). Phantom models used were the optical phantom (OP), light skin (LS), medium skin (MS), and dark skin (DS) models.

Study	Photon energy	Medium	θ_{in} (deg)	Field size
(i)	6-MV mono.	LS, OP	0 to 70	pencil
(ii)	6-, 10-, and 18-MV poly.	LS, MS, DS, OP	0	pencil

a $100 \times 100 \times 100 \text{ cm}^3$ box. In each simulation, the Cerenkov photons of wavelengths from 400 to 800 nm that escaped the medium surface were scored and the initial position, initial direction, final position, final direction, and wavelength were recorded. In addition, the number of photon interactions (scattering or absorption) occurring before the Cerenkov photon escaped was also recorded. Taking a histogram of the initial depth of emission (Z_i -position) allowed for the determination of the sampling depth for each medium.¹⁶ The detection sensitivity was found as the logarithm of the normalized Z_i histogram, and the sampling depth was determined as the depth from which 63% ($1 - 1/e$) of the photons originate. CSF simulations were run with 8×10^8 histories to minimize statistical uncertainties.

For the perturbation analysis, two additional simulations were performed separately from studies (i) and (ii). The first simulation was for scoring of the DSF in the voxelized phantom. The dose delivered to the solid phantom by an incident pencil beam with the same photon energy spectra as those used in study (ii) was scored in voxels of $0.2 \times 0.2 \times 2.0 \text{ mm}^3$. The DSF function was then calculated as the dose delivered to a plane at the depth of $d_0 = 10 \text{ mm}$.

The second simulation was done to obtain the dose delivered to a plane at the depth of $d_0 = 10 \text{ mm}$ for a 6-MV photon beam with a field size of $5 \times 5 \text{ cm}^2$. This simulation utilized the 6-MV phase space data of a TrueBeam linac to match the experimental results. The phase space data were obtained from Varian Medical Systems (Palo Alto, CA, USA). Dose simulations were run with 1×10^{10} histories to keep the dose uncertainty at $<1\%$.

3.2 Simulated Material Properties

Four different materials were used throughout simulations: light, medium, dark-pigmented stratified human skin, and a homogeneous optical phantom. The homogeneous optical phantom was created in simulations based upon a real phantom used in the imaging experiments. The optical phantom was purchased from INO (Ontario, Canada). The optical properties of this phantom were generated from the factory-tested coefficients provided by the company.^{25,26} The absorption and reduced Mie scattering coefficients had values of $\mu_a = 0.3 - 0.0002 \times (\lambda - 450) \text{ cm}^{-1}$ and $\mu'_s = 114.0 \text{ cm}^{-1}$, respectively. The index of refraction of the optical phantom was $n = 1.40$ for wavelengths from 400 to 800 nm.

The optical properties of the stratified human skin models were generated from the descriptions and equations given by Meglinski.²⁷ The absorption properties of the human skin models were found as a linear combination of the individual tissue components: oxygenated hemoglobin, deoxygenated hemoglobin, water, and percent melanin content in each individual skin layer. The reduced Mie scattering coefficients used for the skin layer models were generated based on equations given by Jacques and Bhandari et al.^{28,29} Table 2 shows the thickness of the skin layers and the index of refraction values used in simulations. Table 3 shows the atomic composition of elements used to create both the skin and optical phantoms, based upon the National Institute of Standards and Technology soft tissue and polyurethane resin models found in the GAMOS library. Figure 2 shows the absorption and scattering coefficients of each skin layer within the tissue models alongside the coefficients of the optical phantom.

Table 2 The thickness and refractive index of individual skin layers used in the stratified skin model.

Skin layer	Name	Thickness (mm)	Index of refraction
Epidermis	Stratum corneum	0.02	1.50
	Living epidermis	0.08	1.34
Dermis	Papillary dermis	0.15	1.40
	Upper net dermis	0.08	1.39
	Reticular dermis	1.50	1.40
Subcutaneous	Deep net dermis	0.10	1.38
	Subfat	6.0	1.44

Table 3 The atomic composition of the stratified skin model and optical phantoms.

Optical phantom $\rho = 1.04$ (g/cm ³)		Stratified skin $\rho = 1.06$ (g/cm ³)	
Element	Percent	Element	Percent
H	0.074	H	0.102
C	0.467	C	0.143
N	0.0156	N	0.034
O	0.3352	O	0.708
Mg	0.0688	Na	0.002
Al	0.014	P	0.003
Cl	0.0024	S	0.003
B	0.0226	Cl	0.002
		K	0.003

3.3 Scoring and Fitting of Cerenkov Scatter Function

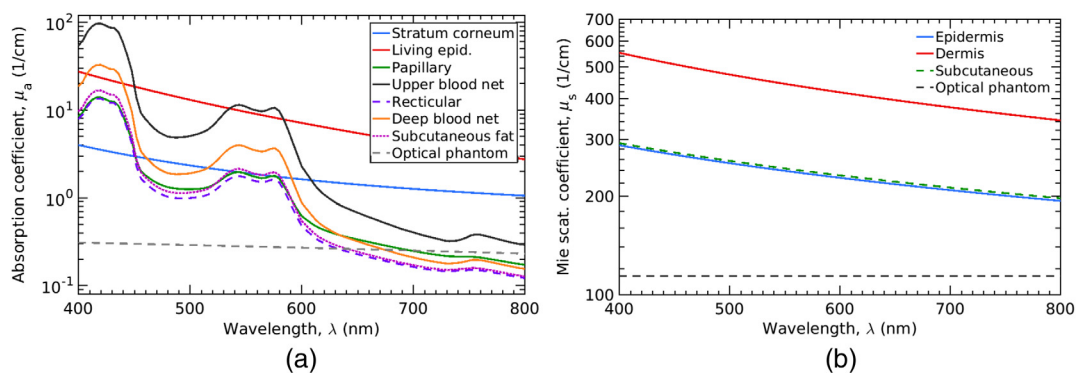
CSFs were generated by the binning and scoring of all surface-escaped Cerenkov photons in studies (i) and (ii). An $8 \times 8 \text{ cm}^2$, 350×350 bin grid was used to create a histogram of the Cerenkov photon flux on the simulated medium surface. To model the CSF for 0-deg incident beams, the histogram was sampled along a line from $r = -20$ to 20 cm using spoke-sampling centered at the origin of the pencil beam on the medium surface. The sampling angle, θ_s , was defined on the medium surface as the rotation from the $+Y$ -axis about the Z -axis. A diagram illustrating the spoke-sampling schema can be seen in Fig. 3(a). The CSF was sampled at the angles of $\theta_s = 0$ to 179 deg with 1-deg increments. The mean of all samples was fitted using a triple-Gaussian distribution with Eq. (4):

$$\text{CSF}_{\text{mean}}(A, B, C, D, E, F, r) = Ae^{-\frac{(r)^2}{B^2}} + Ce^{-\frac{(r)^2}{D^2}} + Ee^{-\frac{(r)^2}{F^2}}, \quad (4)$$

where CSF_{mean} is the average of the CSF cross-sections over θ_s . Parameters A , B , C , D , E , and F are the fit coefficients, and r is the radial distance from the entrance point of the pencil beam on the medium surface. The error in CSF_{mean} was found as the standard deviation at each radial point from the CSF cross sections. The large number of MC histories ensured that the error at each point on CSF_{mean} was $<1\%$ of the maximum value for each CSF. The fitting was performed on CSF_{mean} in MATLAB (Mathworks) using the fitlm function. This function also provides the standard error in the individual fit coefficients. A single- and double-Gaussian, with and without central offset terms, in addition to a Cauchy-Lorentz distribution were also tested; however, a triple-Gaussian without offset yielded the best fit overall. An example of a fit can be seen in Fig. 3(b). The coefficients A , C , and E were scaled based upon the number of primary particles used to generate the CSFs. The amplitude and full-width at half-maximum (FWHM) were found for each normally incident CSF.

3.4 Imaging Experiments

An imaging experiment was performed to measure a $5 \times 5 \text{ cm}^2$ Cerenkov photon image on the optical phantom. Cerenkov images were captured using a Canon electro-optical system (EOS) 5-D commercial camera equipped with CMOS sensors


Fig. 2 The (a) absorption and (b) Mie scattering coefficients of the light stratified skin model and optical phantom. For the medium and dark skin models, the living epidermis has more absorption due to a higher melanin content but other coefficients remain the same.

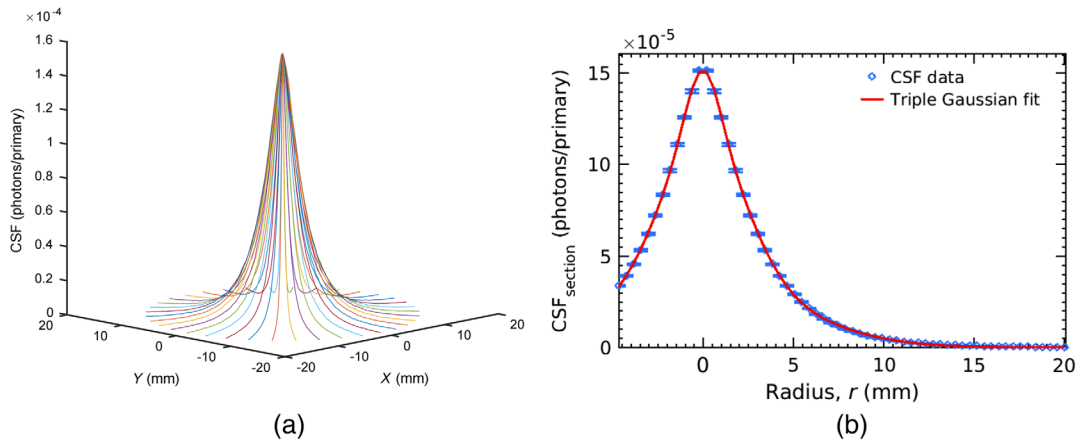


Fig. 3 Visualization of the (a) spoke sampling and (b) fitting of the CSF for a 6-MV polyenergetic beam incident on an optical phantom model. Error bars shown on the CSF in (b) are all $<1\%$ of the maximum value.

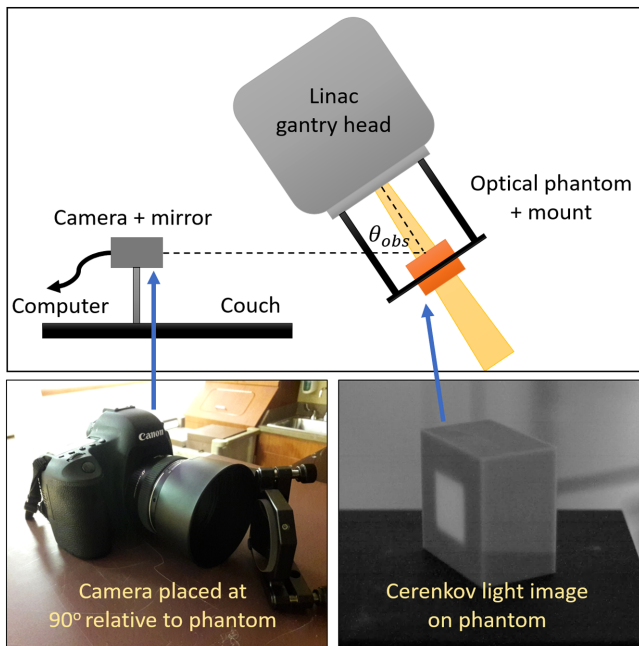


Fig. 4 The experimental setup used to image Cerenkov photons during EBRT. A commercial CMOS camera was placed behind shielding on the treatment couch. A mount was connected to the gantry head that held the optical phantom used throughout the imaging experiment. Cerenkov photon images were taken with the room lights off, and subsequently time and spatial filtered after acquisition.

and an F -number 1.4 lens (Canon USA, Huntington, New York). The optical phantom mentioned in Sec. 3.2 was used in the experiment. Photos and a diagram of the experimental setup can be seen in Fig. 4. The optical phantom was mounted to the gantry head of a TrueBeam linear accelerator. The mount kept the imaged surface of the optical phantom normal to the radiation beam at all times. The optical phantom surface was placed at 100-cm source-to-surface distance. The camera was placed at a distance of 100 cm from the optical phantom surface and the imaging angle was $\theta_{\text{obs}} = 45$ deg. The camera was controlled using the default commercial software, EOS Utility (Canon USA), which allowed for remote shooting through a universal serial bus cable on a laptop computer placed at

the linac control console. A custom camera mount was used to place a 45-deg mirror between the camera and the phantom. This was used to reduce stray radiation in the projection area of the CMOS detector and enabled us to place the camera behind lead shielding. The room was darkened as much as possible to reduce stray ambient photons to the camera.

Individual Cerenkov images were taken with an exposure time of $1/6''$ at 1000000 ISO. The beam parameters used on the linac were a 6-MV beam energy with a 600 MU/min dose rate and 5×5 cm² field size. Each Cerenkov image was processed using both temporal and spatial filtering. Ten images were used to create a composite average image. This image was spatially filtered using a 15-pixel mean filter. The image was then perspective corrected, as described in previous Cerenkov imaging studies.^{20,21,30} No spectral correction was applied to the Cerenkov images based upon the quantum efficiency of the camera as this study utilizes relative dosimetry.

3.5 Perturbation Analysis

Perturbation analysis was done to measure the effects of changing the amplitude and shape of the CSF and the incident beam angle on the fluence and dose images. It was performed using the Cerenkov photon image of the 6-MV photon beam with a 5×5 cm² field size taken with the optical phantom as discussed in Sec. 3.4. The CSF distribution of the optical phantom with a 6-MV photon beam as described in Sec. 3.3 was used for the perturbation analysis. The triple-Gaussian function representing the CSF was remapped to create a radially symmetric distribution. Remapping was done through the creation of a square matrix, with the same size and dimensions as the experimental Cerenkov photon image, with individual elements representing an increasing radial distance from the center of the matrix. The CDSF was also obtained following Eq. (2) with the DSF calculated from Sec. 3.3.

The CSF and CDSF were used to deconvolve the 5×5 cm² Cerenkov photon image to obtain the beam fluence on the surface of the medium and the dose image at a 10-mm depth by Eqs. (1) and (3). Initial fluence and dose images were first obtained using an unaltered CSF shape. These images served as references, which could be compared against fluence and dose images obtained after scaling the amplitude and shape of the CSF. Scaled CSFs were generated by scaling the

triple-Gaussian fit coefficients. Scaling the Gaussian amplitude coefficients A , C , and E by a single value allowed for modification of the total CSF-amplitude. Scaling the Gaussian width coefficients B , D , and F by a single value allowed for modification of the total CSF-FWHM. The scaled CSFs, either in their FWHM or amplitude, were used to again solve for the beam fluence and dose. The scaled beam fluence and dose images were compared with the unscaled fluence and dose using the mean-squared error (MSE) and the error of the penumbra width. The MSE of images was calculated using the image function in MATLAB, which was given as follows:

$$\text{MSE} = \frac{1}{NI_{\max}} \sum_{n=1}^N [I_{\text{scaled}}(n) - I_{\text{unscaled}}(n)]^2, \quad (5)$$

where n is the index of individual image pixels, N is the total number of image pixels, I_{scaled} is the scaled image, I_{unscaled} is the unscaled image, and I_{\max} is the maximum value of I_{unscaled} for normalization. The error in the penumbra width was found as follows:

$$\text{Err}_{\text{pen}} = \frac{\text{Pen}_{\text{scaled CSF}} - \text{Pen}_{\text{unscaled CSF}}}{\text{Pen}_{\text{unscaled CSF}}}, \quad (6)$$

where Pen is the measured penumbra in mm from the I_{scaled} and I_{unscaled} . The penumbra width was measured as the distance between the 80% and 20% of the maximum value points, taken from a cross-line profile of the image. Penumbra measurements were found using cross-line profiles taken from the center of each image, found as the mean profile of both the horizontal and vertical directions. The scaled images of dose (as calculated using the CDSF) were also compared with the MC calculation as described in Sec. 3.1.

The resulting MSEs and penumbra errors were used to evaluate the global error introduced in the deconvolution step when using an “incorrect” CSF. The error due to the CSF-amplitude was calculated by the MSE. The error due to the CSF-FWHM was calculated by the penumbra error. The global error was found as the quadrature of these two errors, given as follows:

$$\text{Err}_{\text{global}} = \sqrt{\text{Err}_{\text{pen}}^2 + \text{MSE}^2}. \quad (7)$$

Perturbation analysis was also performed using the nonnormal CSFs ($\theta_{\text{in}} > 0$ deg) obtained from study (i). The beam fluence was calculated using the normal monoenergetic CSF ($\theta_{\text{in}} = 0$ deg) and compared with the beam fluence calculated with deconvolution by non-normal CSFs using gamma analysis. Gamma analysis is a method commonly used for comparison of two fluences or dose distributions, one a reference and the other a query for testing. 2-D gamma analysis was performed using the definition for γ given by Low et al.^{31,32} The gamma passing rate between images was calculated in MATLAB with custom-written software using four criteria: dose difference/distance-to-agreement (DTA) = 3%/0 mm, 3%/1 mm, 3%/2 mm, and 3%/3 mm.

4 Results

4.1 Dependence of the Cerenkov Scatter Function on Beam Parameters

Line profiles of the CSF for a 6-MV polyenergetic photon beam incident on the skin models, as generated by study (ii), can be seen in Fig. 5. As the skin-melanin content increases, the CSF-amplitude decreases.

Figure 6 shows the CSF profiles of the 6-MV monoenergetic photon beam as observed on the optical phantom surface, generated by study (i). The figure also shows the effects of changing the incident beam angle θ_{in} on the shape of the CSF. As the incident angle increases, the CSF becomes elongated in the direction of the beam path. In addition, the peak position of the CSF becomes displaced from the photon beam entrance point. The trend in the displacement was fit and follows the equation $s = 0.62 \tan(\theta_{\text{in}})$, where s is the displacement in the direction of the beam path in mm.

4.2 Dependence of the Cerenkov Scatter Function on Medium Properties

The coefficients of the CSF for light, medium, dark skin, and optical phantom materials are shown in Table 4. These coefficients can be used to generate radially symmetric CSFs for 0-deg incident photon beams of the listed model and beam energy. The goodness-fit, R^2 , was >0.99 for all cases and individual coefficient errors were between 1.46% and 3.90%, indicating a good parameter fitting of the CSF using Eq. (4).

Table 5 shows the amplitude and width of the CSFs of the stratified skin models and optical phantom for $\theta_{\text{in}} = 0$ deg and 6-, 10-, and 18-MV energies. As expected, the CSF-amplitude for a given energy decreases as melanin content increases due to the increased absorption. As beam energy increases, the CSF-amplitude increases due to more dose deposition per primary particle. Additionally, the CSF-FWHM marginally increases with beam energy. However, no particular trend exists in the CSF-FWHM when comparing different skin models at a single energy. The only difference that exists between the skin models is the percent melanin content in the living epidermis. Scattering and absorption of optical photons occurs identically in all other layers of the skin models. Cerenkov photons diffuse in a similar manner when traveling in layers below the living epidermis, but

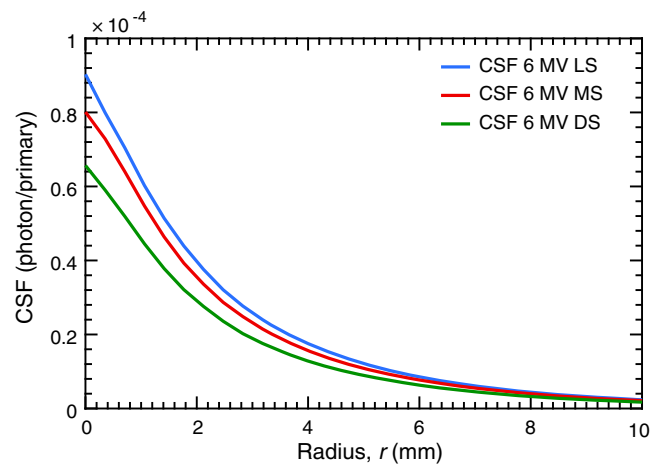


Fig. 5 A profile of the CSFs of light (LS), medium (MS), and dark (DS) skin-layer models at a 6-MV polyenergetic beam energy.

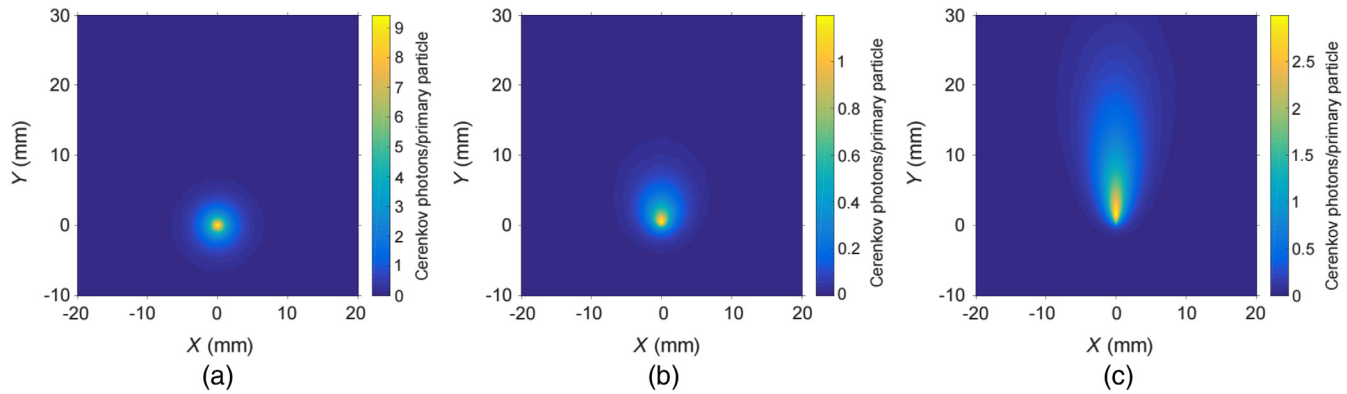


Fig. 6 CSFs of a 6-MV monoenergetic photon pencil beam incident on a stratified light skin model with beam angles: (a) $\theta_{in} = 0$ deg, (b) $\theta_{in} = 35$ deg, and (c) $\theta_{in} = 70$ deg.

Table 4 The coefficients of the CSF for the OP, LS, MS, and DS models for polyenergetic photon beams of TrueBeam linac for $\theta_{in} = 0$ deg. The coefficient errors shown at the bottom represent the range of the individual standard errors for each column.

	A (phot./prim.)	B (mm)	C (phot./prim.)	D (mm)	E (phot./prim.)	F (mm)
6 MV—OP	3.85×10^{-5}	1.34	7.75×10^{-5}	3.28	3.52×10^{-5}	7.11
6 MV—LS	3.53×10^{-5}	0.58	3.92×10^{-5}	1.52	1.55×10^{-5}	3.76
6 MV—MS	3.48×10^{-5}	0.57	3.75×10^{-5}	1.52	1.43×10^{-5}	3.79
6 MV—DS	3.01×10^{-5}	0.58	3.38×10^{-5}	1.50	1.35×10^{-5}	3.74
10 MV—OP	4.55×10^{-5}	1.38	8.81×10^{-5}	3.45	4.05×10^{-5}	7.46
10 MV—LS	3.78×10^{-5}	0.58	4.23×10^{-5}	1.55	1.71×10^{-5}	3.90
10 MV—MS	3.73×10^{-5}	0.62	3.86×10^{-5}	1.60	1.55×10^{-5}	3.95
10 MV—DS	3.63×10^{-5}	0.64	3.37×10^{-5}	1.68	1.29×10^{-5}	4.06
18 MV—OP	4.64×10^{-5}	1.40	9.22×10^{-5}	3.51	4.24×10^{-5}	7.61
18 MV—LS ^a	5.94×10^{-5}	0.82	3.69×10^{-5}	2.88	—	—
18 MV—MS ^a	5.66×10^{-5}	0.82	3.46×10^{-5}	2.88	—	—
18 MV—DS ^a	5.14×10^{-5}	0.82	3.15×10^{-5}	2.89	—	—
Coeff. error (%)	1.46 to 3.78	1.01 to 2.26	1.32 to 2.95	1.27 to 1.85	2.85 to 3.90	1.17 to 1.39

^aThe third Gaussian term has an amplitude statistically consistent with zero, a double Gaussian is sufficient for modeling the 18-MV skin distributions.

with differing levels of absorption between the skin models for Cerenkov photons exiting the tissue. This results in a similar CSF-FWHM for all skin models at a single energy. The CSF-amplitude of the optical phantom was overall greater than that of the skin model. In addition, the CSFs of the optical phantom exhibited more lateral spread than that of any stratified skin models. Both of these results were due to the lower absorption coefficients seen in the optical phantom, allowing for more photons to exit from the phantom and further from the entrance point of the pencil beam.

Figure 7 shows the spectra, number of photon interactions, and detection sensitivity of surface-escaped Cerenkov photons. Figures 7(a)–7(c) show the results for the light-, medium-, and dark-stratified skin models. The light skin shows higher counts of photons at the wavelength of 500 and above 600 nm than

darker skin types. This is due to lower absorption of photons in this wavelength range due to decreased melanin content. The number of photon interactions before escaping the medium showed a similar trend for all skin types. The detection sensitivity trend was also similar for all skin types. Figures 7(d)–7(f) show the results of the optical phantom for 6-, 10-, and 18-MV polyenergetic beams. The trend of energy spectra and the number of interactions for all three energies is similar, with 18-MV displaying the highest counts among the three energies. The detection sensitivity changes with energy due to the difference in primary photon attenuation among the different energies.

Table 5 also shows the sampling depth for each energy in the different materials. At each energy, the sampling depth increases with the skin-melanin content. This result agrees with what was shown by Zhang et al.,³⁰ for the sampling depth of electron

Table 5 The amplitude, FWHM, and the sampling depth of the CSF for the OP, LS, MS, and DS models for 6-, 10-, and 18-MV polyenergetic beams.

	Amplitude (phot./prim.)	FWHM (mm)	Sampling depth (mm)
6 MV—OP	1.54×10^{-4}	5.01	5.26
6 MV—LS	1.01×10^{-4}	1.69	3.11
6 MV—MS	9.53×10^{-5}	1.67	3.13
6 MV—DS	8.58×10^{-5}	1.69	3.16
10 MV—OP	1.79×10^{-4}	5.22	5.77
10 MV—LS	1.08×10^{-4}	1.65	3.35
10 MV—MS	1.02×10^{-4}	1.64	3.36
10 MV—DS	9.34×10^{-5}	1.62	3.40
18 MV—OP	1.86×10^{-4}	5.33	6.02
18 MV—LS ^a	1.11×10^{-4}	1.64	3.46
18 MV—MS ^a	1.04×10^{-4}	1.64	3.48
18 MV—DS ^a	9.39×10^{-5}	1.67	3.52

^aThe third Gaussian term has an amplitude statistically consistent with zero, a double Gaussian is sufficient for modeling the 18-MV skin distributions.

beams on a similar skin model. The sampling depth also increases with the beam energy. This can be explained by the presence of a larger build-up region for higher energy photon beams.

4.3 Effect of Perturbation of the Cerenkov Scatter Function on Deconvolved Fluence and Dose

Figure 8 shows the experimental Cerenkov image and beam fluence line profiles for various CSF-FWHM. Figure 8(a) shows the experimental Cerenkov image taken with a $5 \times 5 \text{ cm}^2$ 6-MV beam incident on the optical phantom. Figure 8(b) shows the Cerenkov photon image given in Fig. 8(a) deconvolved with the CSF for $\theta_{in} = 70$ deg of the optical phantom. Here, the effect of using an incorrect CSF for the deconvolution is shown. The Cerenkov image was taken with a uniform, unmodulated field; therefore, a uniform fluence image is expected. But deconvolution with the CSF of $\theta_{in} = 70$ deg yields a gradient fluence due to the elongation of the CSF. Figure 8(c) shows the CSF using the triple-Gaussian formula for the 6-MV polyenergetic photon beam with the optical phantom. This figure also shows the change in the CSF shape as the FWHM was scaled by multiplying the fit coefficients B , D , and F with the same value. Figure 8(d) shows the effect of scaling the CSF-FWHM on the crossline profile of the beam fluence. Here, it is observed that a wider CSF ($1.3 \times \text{FWHM}$) pushes the penumbra region toward the center of the beam. A narrower CSF ($0.7 \times \text{FWHM}$) results in a steeper penumbra region. This figure shows the impact of the CSF shape on the deconvolution process.

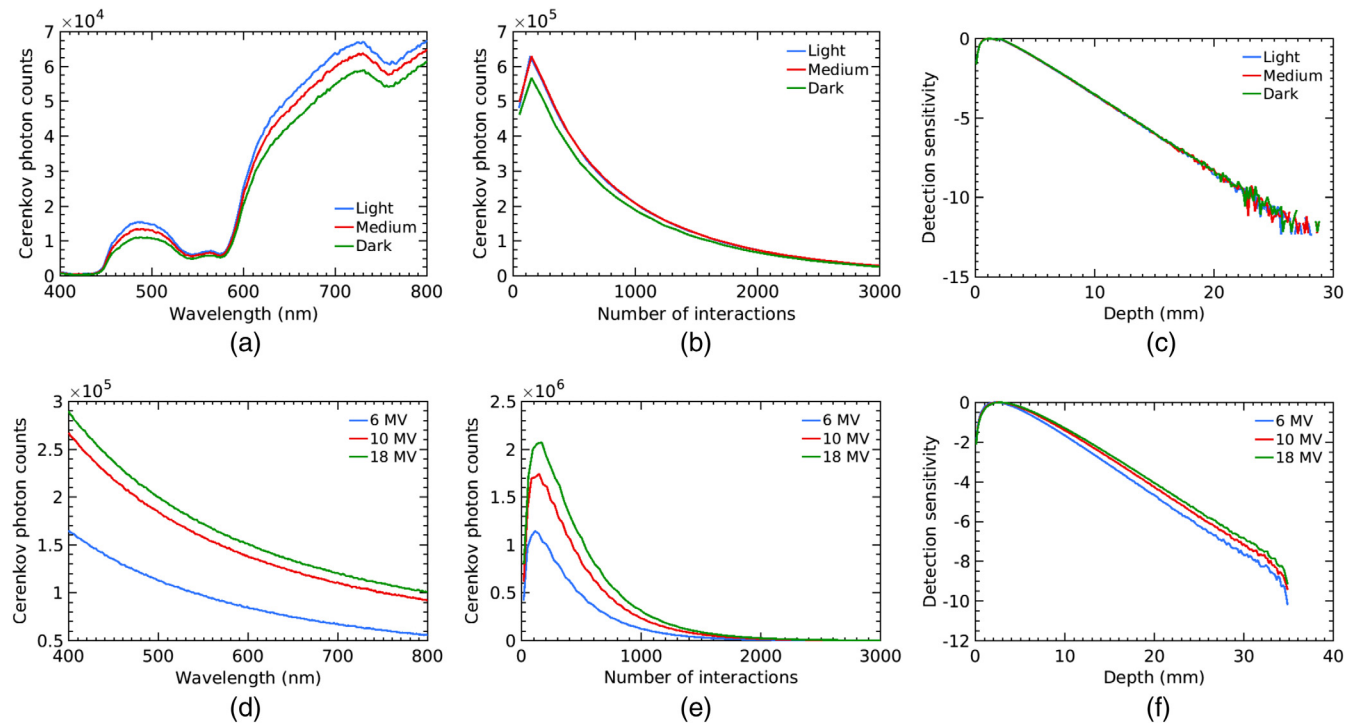


Fig. 7 Cerenkov photon physical statistics from study (ii) for the optical phantom and stratified skin models. (a) and (d) The spectrum of Cerenkov photons emitted from the surface. (b) and (e) The number of photon interactions (scattering and absorption) occurring before the material surface. (c) and (f) The detection sensitivity of the escaped Cerenkov photons. Note (a–c) are taken from the stratified skin models and show results from light, medium, and dark skin types for a 6-MV polyenergetic beam; (d–f) are taken from the optical phantom and show results from 6-, 10-, and 18-MV polyenergetic beams.

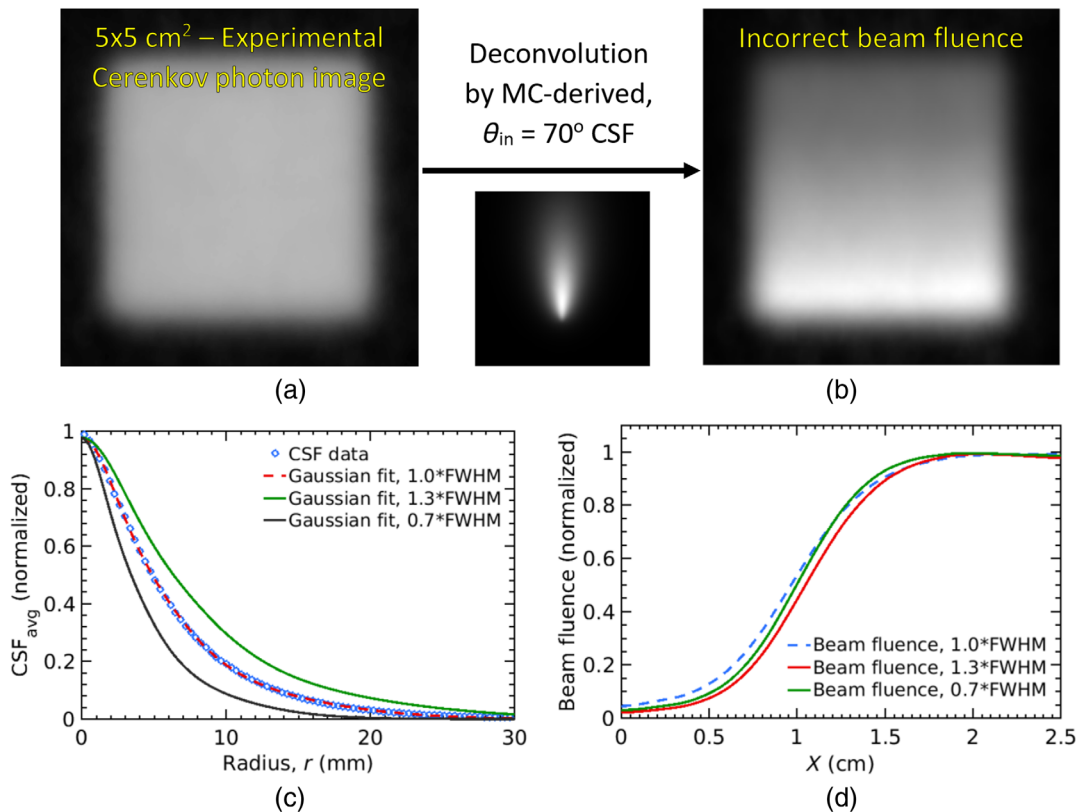


Fig. 8 (a) The experimental Cerenkov photon image taken with a $5 \times 5 \text{ cm}^2$ 6 MV polyenergetic photon beam incident on the optical phantom. This image has been perspective corrected, then temporally and spatially filtered to remove stray radiation noise. (b) Here, the image in (a) has been deconvolved with the incorrect CSF. This image was deconvolved by the monoenergetic $\theta_{\text{in}} = 70\text{-deg}$ CSF. This image represents the beam fluence according to Eq. (1); however, here it is purposefully incorrect for the perturbation analysis. (c) A cross section of the CSF from the 6-MV polyenergetic beam with a triple-Gaussian fit. The FWHM of the fit was scaled and overlaid, as shown. (d) The response of the fluence profile to changes in the CSF-FWHM; (a) deconvolved by the CSFs portrayed in (c).

Figure 9 shows the results of the perturbation analysis with varying CSF-FWHM, CSF-amplitude, and the beam incident angle. For Figs. 9(a)–9(d), the CSF-FWHM and CSF-amplitude were varied relative to the CSF of the 6-MV photon beam with the optical phantom. Figures 9(a), 9(b), 9(d), and 9(e) used the $5 \times 5 \text{ cm}^2$ 6-MV optical phantom fluence image as the reference for calculations, i.e., Fig. 8(a) deconvolved by the 6-MV CSF of the optical phantom. Figure 9(c) used the MC calculated dose at a depth of 10 mm as the reference image.

Figure 9(a) shows the MSE when modifying the CSF-FWHM. For relative CSF-FWHM values <0.5 , the CSF becomes more like a δ -function; therefore, the MSE shows less variability in this region. The MSE in the deconvolved image increases exponentially for relative CSF-FWHM values >1 . Figure 9(b) shows the penumbra error, Err_{pen} , and displays a similar trend to that shown in Fig. 9(a), but also shows an unexpected second minimum at a relative CSF-FWHM of 0.5.

Figure 9(c) shows the MSE when modifying the CSF-FWHM in comparison with MC calculated dose. This figure shows three lines for three different convolution functions: deconvolution by the CSF (Decon. by CSF), deconvolution by the CDSF (Decon. by CDSF), and deconvolution by a δ -function (Decon. by δ). Note that the δ -function deconvolution represents the raw experimental Cerenkov photon image, yielding a constant value for comparison purposes. The MSE reaches a minima at a relative CSF-FWHM of 0.60 for the scaled fluence

image and 0.75 for the scaled dose image. According to our formulation, the minimum value of the scaled dose image trend should lie at a relative CSF-FWHM of 1. However, because an experimental dose image is compared with MC calculated dose, any discrepancies or unaccounted for physical effects in the MC simulation will modify the location of the minimum value in this trend. For example, not accurately representing the complex micro-surface structure that exists on the experimental optical phantom in the simulation will lead to discrepancies in the results. The surface microstructure will realistically modify the CSF shape, which may slightly change the shape and profile of the deconvolved dose image.

Additionally, if the PSF of the imaging system is not ideal, blur may exist in portions of the experimental Cerenkov photon image used in deconvolution. Imaging blur leads to further spreading out of photons in the Cerenkov image, which in turn widens the CSF or CDSF beyond, what would be required of an ideal imaging system. Therefore, blur or a nonideal imaging system would shift the minimum value of the trends in Fig. 9(c) to the right, to a relative CSF-FWHM >1 . Because these trends reach a minimum at a relative CSF-FWHM <1 , the experimental imaging system used was close enough to an ideal or diffraction-limited case and the simplification used on Eq. (1) was valid.

The scaled dose image trend in Fig. 9(c) is expected to reach a minimum value closer to a relative CSF-FWHM of 1 in

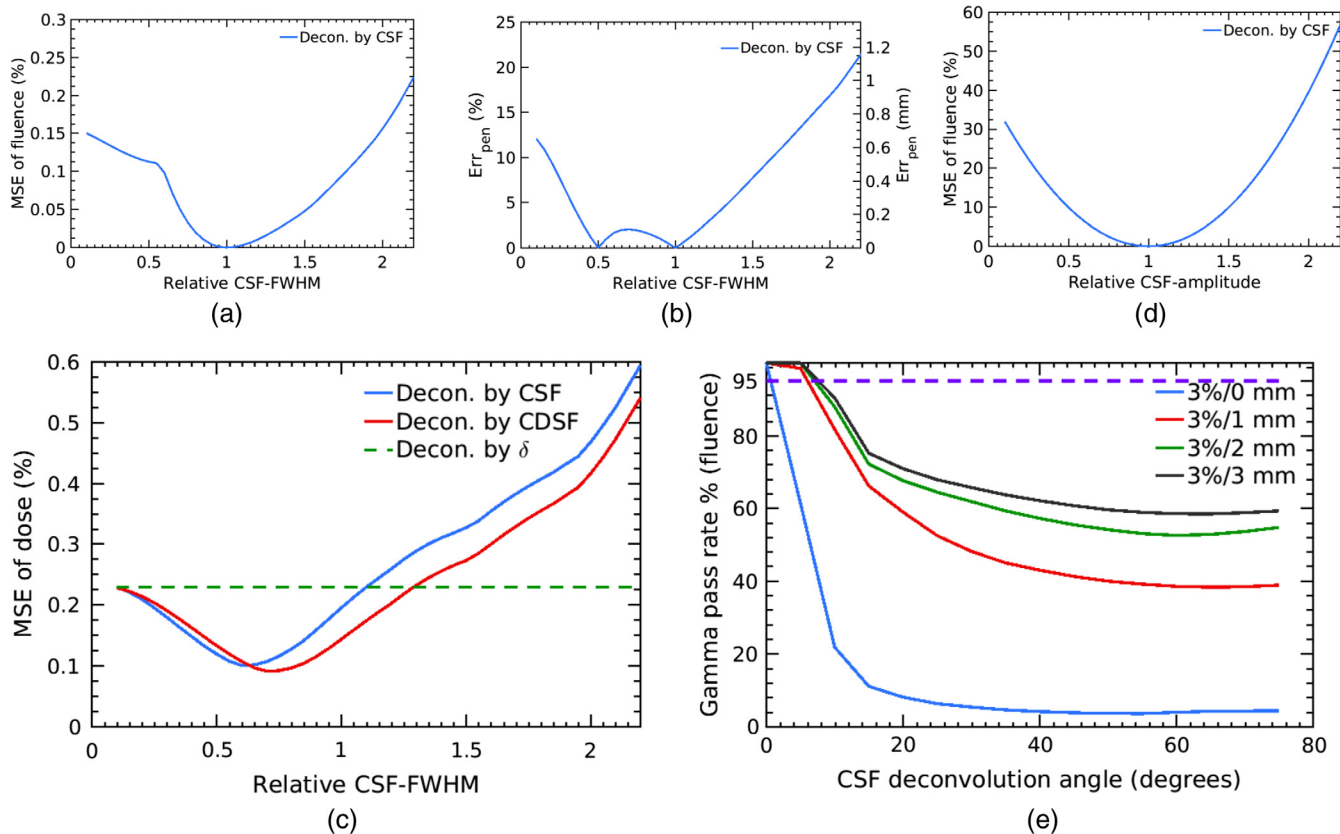


Fig. 9 The results of the perturbation analysis. (a) The MSE of the beam fluence with respect to itself when modifying the CSF-FWHM. (b) The penumbra error for the fluence image when modifying the CSF-FWHM. (c) The MSE of the various images with respect to the MC calculated dose for the same field size, beam energy, and optical phantom model. This image shows three trendlines: deconvolution by the CSF representing the fluence image, deconvolution by the CDSF representing the dose image, and deconvolution by a δ -function representing the raw experimental image. (d) The MSE of the fluence image with respect to itself when modifying the amplitude of the CSF. (e) The gamma passing rate of the fluence image in comparison to the CSF of $\theta_{in} = 0$ deg when changing the entrance angle of the CSF used in deconvolution as shown in Fig. 6.

comparison with the scaled fluence image. The CDSF is calculated from deconvolution of the CSF by the DSF. In general, for superficial dosimetry ($d < d_{max}$), the DSF will be very narrow in comparison with the CSF.²⁰ Because of this, the CDSF will retain the overall shape of the CSF but will be sharpened slightly. This effect is shown in the similarity between the MSE trends of the scaled dose and scaled fluence images. The fact that the MSE with CDSF is smaller than the MSE with CSF and is closer to a relative CSF-FWHM of 1 implies that the use of CDSF for dose estimation from the raw Cerenkov image is the correct approach. Figure 9(c) also shows that the MSEs of the fluence and dose images fall below the value of the raw experimental image trend. This shows the validity of our mathematical approach in solving for and improving the light-to-dose correlation.

Figure 9(d) shows the MSE when varying the CSF-amplitude. The trend in this error is seen as a simple parabolic curve. Changes to the CSF-amplitude will result in an exponential increase in the magnitude of the fluence image after deconvolution.

Figure 9(e) shows the gamma passing rate when changing the angle of the CSF. The passing rate decreases sharply beyond an angle of $\theta_{in} > 6$ deg for all gamma criteria with a DTA ≥ 1 mm. This is primarily due to the gradient created across center of the field for increasing values of θ_{in} as seen

in Fig. 8(b). The gamma passing rate decreases much more quickly for the 3%/0 mm criteria, as this is strictly a measure of the dose difference between the images. The gamma passing rate flattens out beyond $\theta_{in} > 45$ deg for all gamma criteria with a DTA ≥ 1 mm. For this region, the dark areas just beyond the penumbra will still have acceptable passing rates, which creates the baseline passing value observed.

Figure 10(a) shows a map of the global error determined by Eq. (7) as the function of CSF-amplitude and CSF-FWHM. Also shown in Fig. 10(a) are the points of CSFs for various photon energies and medium types as given in Table 5. The cluster of points in the bottom left represents the CSFs of the stratified skin models at 6-, 10-, and 18-MV polyenergetic photon beam energies. The three points on the top right represent the CSFs of the optical phantom at the three beam energies. Overlaid on this map is a topographic representation of the global error, relative to the 6-MV light skin CSF data point. The CSFs of all skin models lie within a 1% global error from one another. Using the CSF of any skin model in deconvolution yielded an almost identical result when comparing the penumbra shape or image magnitude. However, the application of the CSF of the optical phantom to a Cerenkov image captured from any stratified skin yielded a $>38\%$ error in the deconvolved image. Figure 10(b) shows an expanded view of the CSFs of the stratified skin model data points shown in Fig. 10(a).

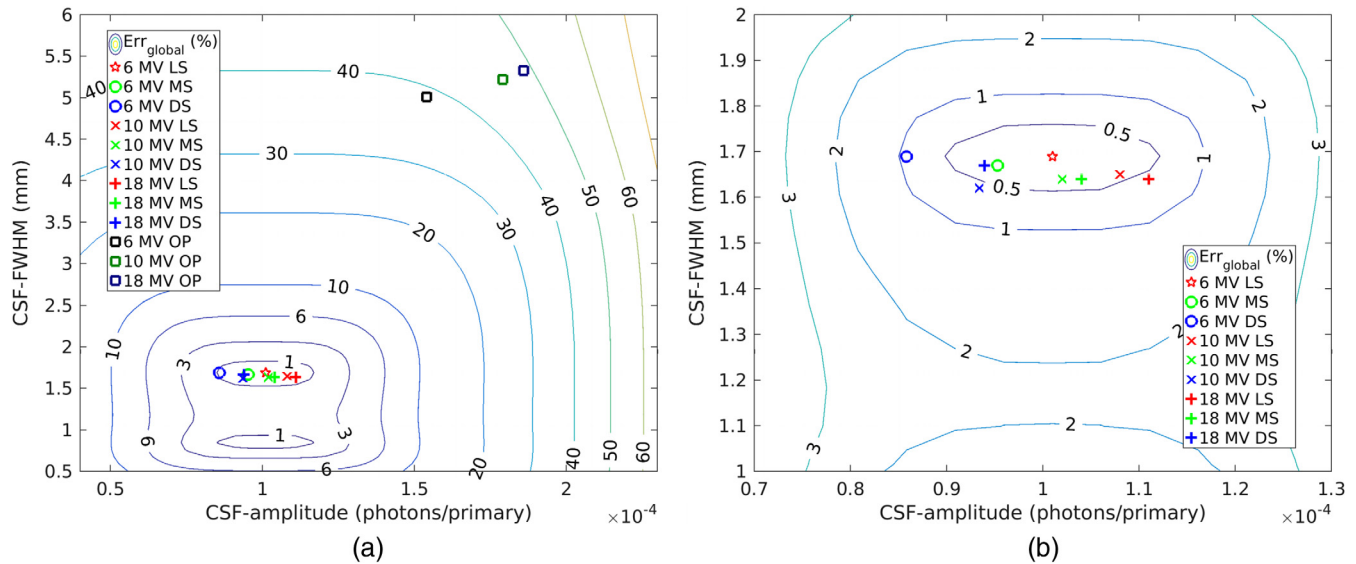


Fig. 10 (a) A map of the FWHM and amplitude of CSFs generated for the optical phantom (OP), light skin (LS), medium skin (MS), and dark skin (DS) models for 6-, 10-, and 18-MV polyenergetic beams. Overlaid on this map is the global error in the deconvolution process relative to the 6-MV light skin CSF data point denoted by a star. The global error was generated as the quadrature of the error in the penumbra measurement for the CSF-FWHM axis and the MSE for the CSF-amplitude axis. The global error displays what the error in the deconvolution product image when using an incorrect CSF. (b) An expanded view of the skin model CSFs shown in (a).

5 Discussion

The global error shown in Fig. 10 was calculated using two separate metrics. Both the penumbra errors due to CSF-FWHM and the MSE due to CSF-amplitude reflect the changes in the deconvolved images that we are primarily interested in quantifying. Modifying the CSF-FWHM alone changes the response of the high gradient regions in the deconvolved image, such as the penumbra. Modifying the amplitude alone changes the overall image magnitude but does not modify the image profile. Using the MSE as a metric for the CSF-FWHM does not capture the direct effect on the penumbra. Using the penumbra error as the metric for the CSF-amplitude does not capture the direct effect on the magnitude of the whole image. Therefore, we choose to use these two different metrics in one formulation, Eq. (7), to give a relative estimate of the global error that we expect to see when deconvolving with an incorrect CSF.

In this paper, the effects of the measurement setup parameters on the CSF and the deconvolved image were studied. These included the beam energy, the irradiated material, and the incident beam angle. It was observed that the beam energy had a noticeable effect on the CSF-amplitude and almost no effect on the CSF-FWHM. The 6-MV CSF-amplitude in the light skin model increased by 6.9% and 10% when the beam energy increased to 10 and 18 MV, respectively. This increase propagated the deconvolution process to yield a 0.3% and 0.5% difference in the global error of the product images, respectively. Therefore, using the CSF with an incorrect photon energy in deconvolution is insignificant.

The irradiated material had a large effect on both the CSF-amplitude and CSF-FWHM. For a 6-MV beam energy, changing from a light skin model to the optical phantom increased the CSF-amplitude by 52% and the CSF-FWHM by 196%. This change propagated the deconvolution process to yield a 39% difference in the product image using the global error. The irradiated skin pigment had a small effect on of the CSF-amplitude

and no effect on the CSF-FWHM. For a 6-MV beam energy, changing from light skin to medium or dark decreased CSF-amplitude by 6% and 15%, respectively. This decrease propagated the deconvolution process to yield a 0.2% and 0.9% difference in the global error of product images, respectively. Therefore, using the incorrect CSF material has a significant effect on the deconvolved images; however, using the CSF of an incorrect skin type in deconvolution is insignificant.

The result of errors introduced by changing the beam angle is more difficult to evaluate. It was observed that changing the beam angle from 0 deg to 35 deg introduced errors in the deconvolution process that caused the gamma passing rate to decrease to 45%, as per the 3%/1 mm criteria. This effect would be considered very significant. Hence, the shift-invariant assumption used for the current mathematical algorithm is not valid when the incident beam angle change is large. To solve this problem, deconvolution will no longer be performed with a single CSF or CDSF over the whole image. Regions of near-uniform beam angles will be deconvolved by the CSF corresponding to that similar beam angle following piece-wise deconvolution techniques. Under this analysis, we conclude that to minimize the error in the deconvolution product, the range of angles used in a single area of deconvolution should be no more than $\Delta\theta_{in} = 6.04$ deg, as per the 3%/1 mm gamma criteria. This constraint will keep the gamma passing rate above 95% for that region. This result can be used to partition an image into regions bounded by a difference in the beam entrance angle before piece-wise deconvolution is performed.

6 Conclusions

In this study, the CSF was characterized. The CSF was found in models of light, medium, dark stratified human skin, and an optical phantom for polyenergetic photon beam energies. The CSF was also solved for oblique incident beam angles in both the light skin and optical phantom models. The CSFs of

normally incident beams were fit with a triple-Gaussian function and the coefficients were provided. These coefficients can be used to generate a radially symmetric CSF, which can be used in deconvolution with a measured Cerenkov photon image to find either the beam fluence or dose distribution with a known DSF.

Perturbation analysis was performed to study the sensitivity of the deconvolved images on the shape and amplitude of the CSF, beam energy, incident beam angle, and the type of medium. The CSF-amplitude and FWHM was found to have significant effects on deconvolution. An increase in the CSF-amplitude propagated as an exponential increase in the amplitude of the deconvolved image. An increase in the CSF-FWHM propagated as a near-linear increase in the penumbra width of the deconvolved image. The energy of the beam used to create the CSF was found to be insignificant to the deconvolution process. The angle of the beam used to create the CSF was found to be significant in the deconvolution process. The result suggests the need to move toward piece-wise, shift-variant deconvolution when imaging a beam with multiple entrance angles. The incident beam angle used for the CSF should vary by no more than 6.0 deg for a single region of deconvolution. The material model used to generate the CSF has a significant effect on deconvolution. The CSF from one material should not be used on another. However, the pigment of human skin does not have a significant effect on the deconvolution process. The CSFs of different skin tones can be used interchangeably with a <1% error in the deconvolution product image.

Disclosures

The presented work was funded by a research grant from the University of Minnesota, Department of Radiation Oncology, and the Institute for Engineering in Medicine (IEM). The authors have no potential conflicts of interest to disclose.

Acknowledgments

The authors would like to thank Dr. Adam Green at the University of St. Thomas, MN, for his insight into experimental aspects of the project.

References

1. S. Webb, *The Physics of Three-Dimensional Radiation Therapy*, ch. 2.5, pp. 87–101, Institute of Physics Publishing, Bristol (1993).
2. H. H. Liu, T. R. Mackie, and E. C. McCullough, "A dual source photon beam model used in convolution/superposition dose calculations for clinical megavoltage X-ray beams," *Med. Phys.* **24**, 1960–1974 (1997).
3. P. A. Čerenkov, "Visible radiation produced by electrons moving in a medium with velocities exceeding that of light," *Phys. Rev.* **52**, 378–379 (1937).
4. J. V. Jelley, "Cerenkov radiation and its applications," *Br. J. Appl. Phys.* **6**(7), 227–232 (1955).
5. B. Pogue et al., "Cerenkov imaging in the potential roles of radiotherapy QA and delivery," *J. Phys. Conf. Ser.* **847**, 012046 (2017).
6. J. Andreozzi et al., "TU-AB-BRA-12: quality assurance of an integrated magnetic resonance image guided adaptive radiotherapy machine using Cerenkov imaging," *Med. Phys.* **43**(6), 3736–3736 (2016).
7. J. M. Andreozzi et al., "Cerenkov imaging method for rapid optimization of clinical treatment geometry in total skin electron beam therapy," *Med. Phys.* **43**(2), 993–1002 (2016).
8. P. Black, Y. Na, and C. Wu, "SU-G-1eP4-06: feasibility of external beam treatment field verification using Cerenkov imaging," *Med. Phys.* **43**(6Part27), 3678–3679 (2016).
9. A. Darafsheh et al., "SU-F-J-56: the connection between Cerenkov light emission and radiation absorbed dose in proton irradiated phantoms," *Med. Phys.* **43**(6Part9), 3418–3419 (2016).
10. A. K. Glaser et al., "Projection imaging of photon beams by the Cerenkov effect," *Med. Phys.* **40**(1), 012101 (2013).
11. A. K. Glaser et al., "Three-dimensional Cerenkov tomography of energy deposition from ionizing radiation beams," *Opt. Lett.* **38**(5), 634–636 (2013).
12. Y. Helo et al., "Imaging Cerenkov emission as a quality assurance tool in electron radiotherapy," *Phys. Med. Biol.* **59**(8), 1963–1978 (2014).
13. Y. Roussakis et al., "Real-time Cerenkov emission portal imaging during cyberknife radiotherapy," *Phys. Med. Biol.* **60**(22), N419–N425 (2015).
14. R. Zhang et al., "Cherenkovscopy based patient positioning validation and movement tracking during post-lumpectomy whole breast radiation therapy," *Phys. Med. Biol.* **60**(1), L1–L14 (2015).
15. P. Bruza et al., "Online combination of EPID Cerenkov imaging for 3-D dosimetry in a liquid phantom," *IEEE Trans. Med. Imaging* **36**(10), 2099–2103 (2017).
16. R. Zhang et al., "Beam and tissue factors affecting Cerenkov image intensity for quantitative entrance and exit dosimetry on human tissue," *J. Biophotonics* **10**, 645–656 (2017).
17. D. Shu et al., "Determination of the relationship between dose deposition and Cerenkov photons in homogeneous and heterogeneous phantoms during radiotherapy using Monte Carlo method," *J. Radioanal. Nucl. Chem.* **308**, 187–193 (2016).
18. A. K. Glaser et al., "Optical dosimetry of radiotherapy beams using Cerenkov radiation: the relationship between light emission and dose," *Phys. Med. Biol.* **59**, 3789–3811 (2014).
19. Y. Zlateva, J. Seuntjens, and I. El Naqa, "SU-C-201-07: towards clinical Cerenkov emission dosimetry: stopping power-to-Cerenkov power ratios and beam quality specification of clinical electron beams," *Med. Phys.* **43**(6Part2), 3317–3317 (2016).
20. E. Brost and Y. Watanabe, "A mathematical deconvolution formulation for superficial dose distribution measurement by Cerenkov light dosimetry," *Med. Phys.* **45**(6), 3880–3892 (2018).
21. E. Brost and Y. Watanabe, "Characterization of the Cerenkov scatter function for use in superficial dose measurement from external beam radiation treatments," *Proc. SPIE* **10492**, 104920M (2018).
22. P. Arce et al., "Gamos: a framework to do geant4 simulations in different physics fields with an user-friendly interface," *Nucl. Instrum. Methods Phys. Res.* **735**, 304–313 (2014).
23. A. K. Glaser et al., "A gamos plug-in for geant4 based Monte Carlo simulation of radiation-induced light transport in biological media," *Biomed. Opt. Express* **4**, 741–759 (2013).
24. D. SheikhBagheri and D. W. O. Rogers, "Monte Carlo calculation of nine megavoltage photon beam spectra using the beam code," *Med. Phys.* **29**, 391–402 (2002).
25. T. Moffitt, Y.-C. Chen, and S. Prael, "Preparation and characterization of polyurethane optical phantoms," *J. Biomed. Opt.* **11**, 041103 (2006).
26. J.-P. Bouchard et al., "Reference optical phantoms for diffuse optical spectroscopy. Part 1 - error analysis of a time resolved transmittance characterization method," *Opt. Express* **18**, 11495–11507 (2010).
27. I. V. Meglinski, "Quantitative assessment of skin layers absorption and skin reflectance spectra simulation in the visible and near-infrared spectral regions," *Physiol. Meas.* **23**, 741–753 (2002).
28. S. L. Jacques, "Optical properties of biological tissues: a review," *Phys. Med. Biol.* **58**, R37–R61 (2013).
29. A. Bhandari et al., "Modeling optical properties of human skin using Mie theory for particles with different size distributions and refractive indices," *Opt. Express* **19**, 14549–14567 (2011).
30. R. Zhang et al., "Superficial dosimetry imaging of Cerenkov emission in electron beam radiotherapy of phantoms," *Phys. Med. Biol.* **58**, 5477–5493 (2013).
31. D. A. Low et al., "A technique for the quantitative evaluation of dose distributions," *Med. Phys.* **25**(5), 656–661 (1998).
32. T. Depuydt, A. Van Esch, and D. P. Huyskens, "A quantitative evaluation of imrt dose distributions: refinement and clinical assessment of the gamma evaluation," *Radiother. Oncol.* **62**(3), 309–319 (2002).

Biographies for the authors are not available.